Lateral variability of the estuarine turbidity maximum in a tidal strait

Neil K. Ganju[a,b,*] and David H. Schoellhamer[a,b]

[a] U.S. Geological Survey, Placer Hall, 6000 J Street, Sacramento, CA 95819, USA
[b] University of California, Davis, Department of Civil and Environmental Engineering, One Shields Avenue, Davis, CA 95616, USA
*corresponding author, email: nganju@usgs.gov, phone: 916 278 3117, fax: 916 278 3013

Abstract

The behavior of the estuarine turbidity maximum (ETM) in response to freshwater flow, tidal forcing, and bed dynamics has been studied extensively by many researchers. However, the majority of investigations focus on the longitudinal position and strength of the ETM, which can vary over tidal, spring-neap, and seasonal timescales. ETMs may become longitudinally fixed due to bathymetric constraints, and thus the lateral position may vary significantly on differing timescales. Lateral dynamics of the ETM may affect contaminant uptake in biologically active regions, while local deposition patterns may be affected by the dominant lateral position. A longitudinally fixed ETM in Carquinez Strait, California, was studied to specifically investigate the dynamics of lateral ETM variability during April, 2004. An abrupt topographical control on the north side restricts gravitational circulation resulting in convergence and particle trapping, creating the ETM. The cross-section was continuously monitored with two upward-looking velocity profilers and four optical backscatterance sensors. In addition, cross-sectional measurements over one tidal cycle were performed during a spring tide with boat-mounted velocity and water quality profilers. The lateral and vertical position of the ETM center of mass varied by a maximum of 250 m and 5 m respectively (20% of width and 17% of depth) over the tidal timescale, while tidally averaged lateral and vertical position varied substantially less (50 m and 1 m, respectively). ETM position responded to tidal energy (U_{rms}), with higher vertical position and a laterally centered position resulting from increased mixing during spring tides, and a northerly lateral position during neap tides, when mixing is decreased. Hydrodynamic and sediment transport modeling of this period reproduces the lateral and vertical movement of the ETM center of mass. Modeling results indicate increased gravitational circulation in the Strait and enhanced particle trapping on the north side during neap tides, thus displacing the ETM center of mass to the north. The south side has no topographical control, and therefore no particle trapping mechanism exists on the south side. Secondary circulation is strengthened on spring tides, distributing near-bed sediment towards the south. The field and modeling results are in agreement with previous work in Carquinez Strait, and further elucidate the strong lateral variation of the ETM, even in narrow, energetic tidal straits.

Keywords: turbidity maximum; lateral variability; estuaries; San Francisco Bay

1. Introduction

The estuarine turbidity maximum (ETM) is a feature common to many estuaries, where sediments of marine and/or terrestrial origin converge to form locally increased turbidity. The importance of the ETM arises from its role in sedimentary and biological processes: local deposition is enhanced near the ETM (e.g. Grabemann et al., 1997; Woodruff et al., 2001; Ganju et al., 2004), while biological activity may be focused near the ETM as well (e.g. Kimmerer et al., 1998; Islam et al., 2005). The erosional/depositional nature of the local sediment bed is known to affect benthic community composition (Aller and Stupakoff, 1996), therefore lateral gradients of deposition may create gradients in the benthos.

The mechanism of ETM formation varies depending on the geometry, tidal dynamics, and freshwater flow of an estuary. Some studies cite topographical effects (Jay and Musiak, 1994; Schoellhamer, 2001), tidal asymmetry (Sanford et al., 2001), and cyclical resuspension of temporarily deposited sediment (Grabemann et al., 1997; Ganju et al., 2004), to name a few. One notable study of lateral variability of the ETM was presented by Geyer et al. (1998), where frontal convergence of ebb waters over distinct topography is an important mechanism; a pool of erodible material is preferentially deposited on one side of the estuary, resulting in ETM creation near that location.

The ETM can be thought of as a zone of locally increased turbidity, which has a distinct center of mass, longitudinally, laterally, and vertically. If one assumes that the ETM is longitudinally fixed, then the lateral and vertical variability in a cross-section can be evaluated by monitoring the cross-section laterally and vertically at several points. The lateral and vertical location of this center over differing timescales provides insight into ETM formation and maintenance, and may potentially link with studies of biological activity, benthic community structure, and deposition patterns. This study aims to demonstrate the potential lateral and vertical variability of the ETM over tidal and subtidal timescales, using a combination of field and modeling efforts.

2. Field observations

2.1. Site description

Carquinez Strait connects Suisun Bay (the landward-most subembayment of San Francisco Bay) and San Pablo Bay (Figs. 1,2). Maximum depths in Carquinez Strait approach 30 m, while both Suisun and San Pablo Bay are relatively shallow, with deep shipping channels bisecting shallower areas. The landward end of Carquinez Strait immediately bifurcates at the western boundary of Suisun Bay, near the I-680 Bridge. The northern half of the channel continues northeast into the Reserve Fleet channel and terminates in Grizzly Bay, while the southern half of the channel runs east-northeast along the southern edge of the bay. The two channels are separated by a shallow bar, portions of which are exposed at low tide.

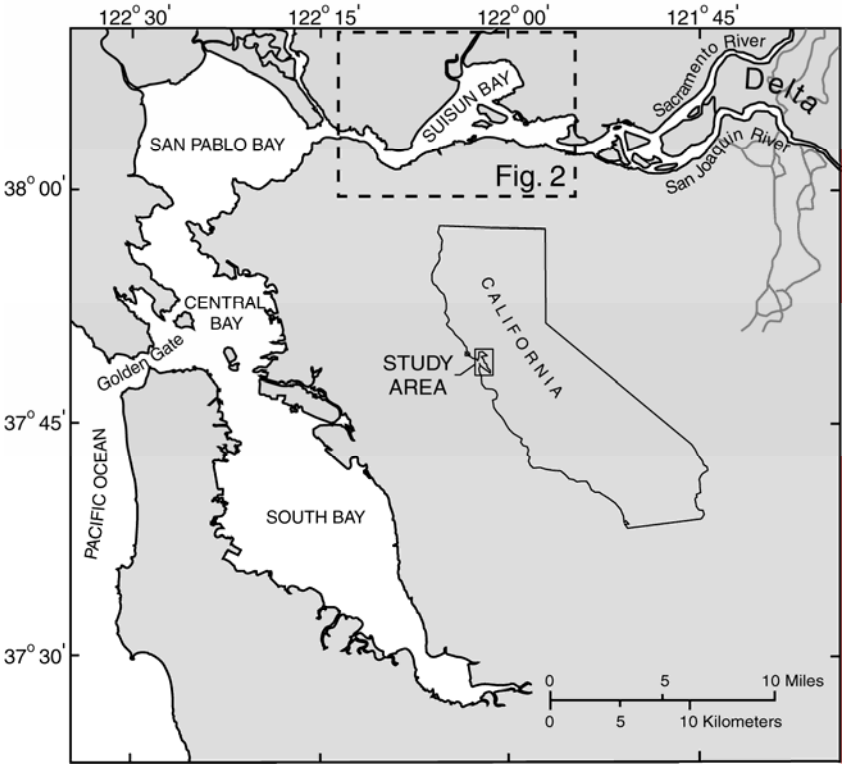

Figure 1. San Francisco Bay and western end of Sacramento/San Joaquin River Delta. Suisun Bay is landward-most embayment in northern San Francisco Bay.

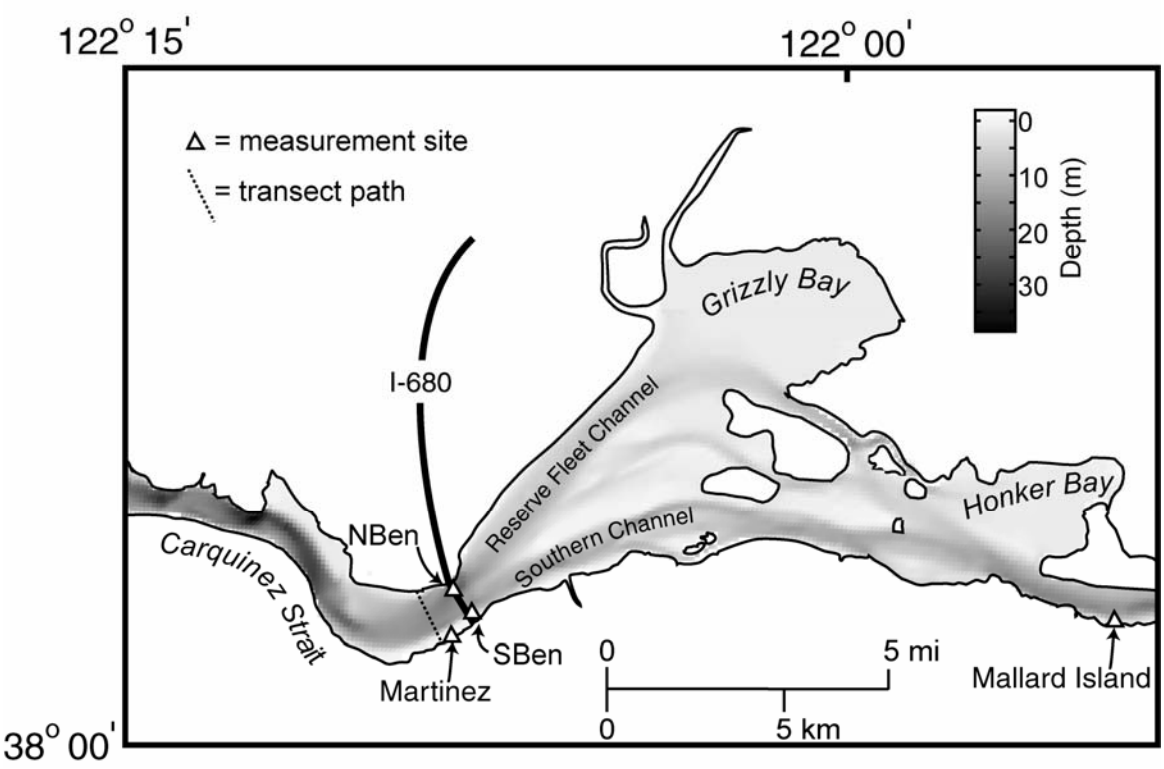

Figure 2. Carquinez Strait and Suisun Bay. Carquinez Strait connects San Pablo Bay and Suisun Bay. Grizzly and Honker Bays are shallow areas of Suisun Bay. Sites NBen and SBen are located on piers of the I-680 Bridge. Depth is referenced to mean lower low water.

The Sacramento/San Joaquin River Delta (Delta) supplies the majority of freshwater to Suisun Bay; freshwater flow is mainly controlled by reservoir releases and water operations within the Delta, and maximum flows are typically in the winter months. Net flow magnitude ranges from near zero to over 16,000 $m^3 s^{-1}$. Flow is managed to keep the 2-isohaline seaward of the Delta during the low-flow season (~May to November). Semi-diurnal tides cause currents exceeding 1 m s^{-1}, with a maximum spring tide range in excess of 2 m.

Previous studies in Carquinez Strait have identified gravitational circulation within Carquinez Strait, especially when the longitudinal salinity gradient is at a maximum (Burau et al., 1993). This helps sustain an ETM that forms at the eastern (landward) end of the strait, due to a sharp bathymetric change. This "sill", which decreases the depth from 18 m to 11 m on the north side, forms a landward control on the gravitational circulation and therefore the ETM (Jay and Musiak, 1994; Schoellhamer, 2001). Gravitational circulation is maximized during neap tides (Burau et al. 1993), and vertical stratification is also maximized during these periods due to reduced vertical mixing. The lateral variability induced by the circulation dynamics is unclear, and an intensive monitoring of the cross-section over subtidal frequencies may reveal the dominant patterns.

2.2. Methods

2.2.1. Continuous monitoring

The U.S. Geological Survey established a continuous monitoring site on the north side of Carquinez Strait, on the I-680 Bridge in 1997 (site NBen; Fig. 2). This site consists of two conductivity, temperature, depth, and optical sensor multiprobes, at a near-bottom (lower) and a mid-depth (upper) elevation. For this study, a second site was established and maintained from March 24, 2004 to July 9, 2004 on the south side (site SBen), also on the I-680 Bridge. Optical sensors were deployed at the same vertical locations as the multiprobes at site NBen. The horizontal distance between sites NBen and SBen is 650 m, while the vertical distance between the upper and lower sensors is 15 m at both sites. Total width of the strait is 1200 m at this location. Fouling and debris interference can reduce data yield from optical sensors,

therefore all sensors were cleaned and checked with known standards during site visits (typically once every three weeks). Water samples were collected to calibrate the optical sensor output to SSC (Buchanan and Ganju, 2005).

Water velocity measurements were collected using upward-looking acoustic Doppler current profilers (ADCPs, 600 kHz broadband, RD Instruments; any use of trade, product, or firm names is for descriptive purposes only and does not imply endorsement by the U.S. Government), deployed on the bed 300 m seaward of the I-680 Bridge, from March 28, 2004 to July 7, 2004. Two units were deployed: one on the north side, and one on the south side. The units were programmed to sample at 10 min intervals, in 0.5 m vertical bins. Due to highly variable bathymetry seaward of the I-680 Bridge, the cross-section monitored by the ADCPs and the cross-section at the Bridge are not identical, which hampers comparison of the two sets of data.

The four optical sensors deployed at the I-680 Bridge each conceptually occupy a quarter of the area between them, in the cross-section (Fig. 3). This ignores the variability within a quadrant or outside the area bounded by the four sensors, but the general trends in SSC should be reflected by these four sensors. After these assumptions, one can compute a center of mass for the ETM by balancing the total mass laterally and vertically. It should be noted that the aspect ratio of Figure 3 suggests that sensor SL occupies an isolated hole; when the cross-section is expanded to its actual proportions, it is clear that the use of sensor SL to represent that portion of the channel is justified.

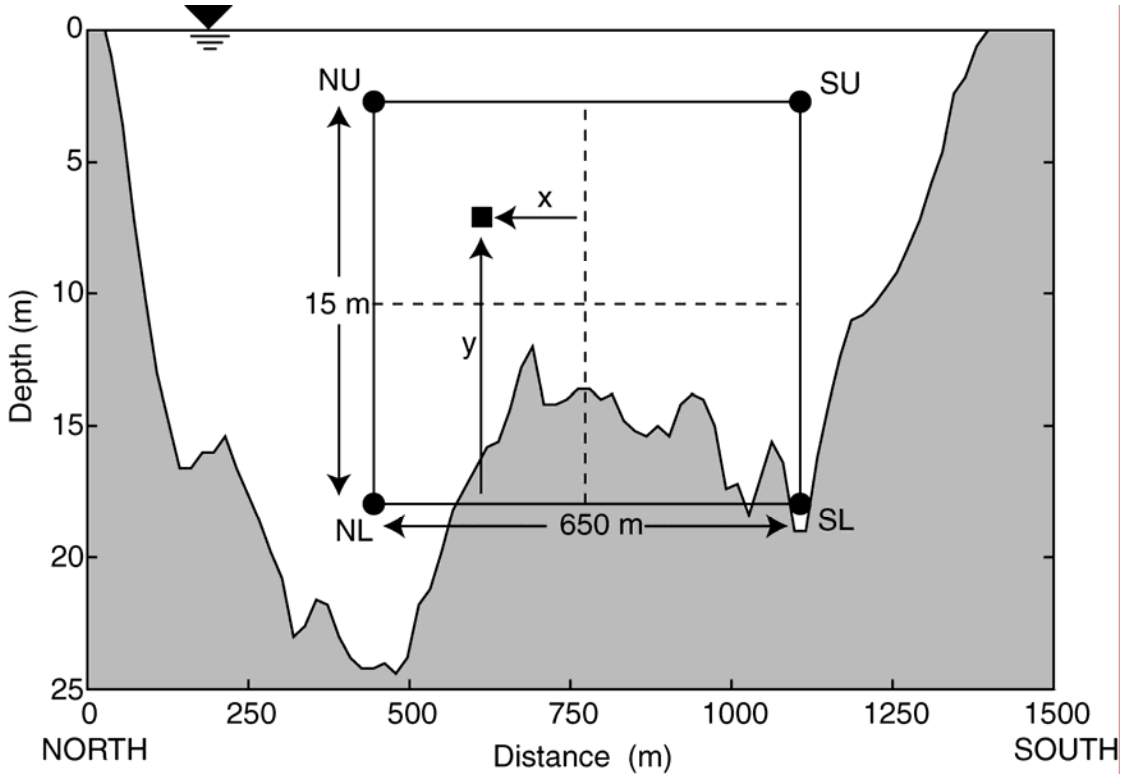

Figure 3. Cross-section of Carquinez Strait at I-680 Bridge. Four optical sensors were situated within the cross-section; upper and lower water column at site NBen (NU and NL respectively) and upper and lower water column at site SBen (SU and SL respectively). Each sensor conceptually represents a 325 m x 7.5 m rectangle of the cross-section. Square indicates example of ETM center of mass, with x and y coordinate origins defined as shown. Depth is referenced to mean lower low water.

2.2.2. Tidal cycle monitoring

Detailed measurements of velocity and SSC were undertaken to find the ETM center of mass. Cross-sectional measurements over one tidal cycle on July 7, 2004 coincided with a spring tide. Velocities were measured using a boat-mounted ADCP that traversed the 1200-m wide channel (1000 m seaward of the I-680 Bridge) every 10-15 min for 12 h. Conductivity, temperature, depth, and turbidity were measured

using a Seabird SBE19plus profiling package, deployed from a second vessel. The second vessel crossed Carquinez Strait every 30-45 min, profiling at 12 nodes in the cross-section. The package was lowered and raised at 1 m s^{-1}, sampling at 4 Hz. Therefore vertical sampling density was approximately 0.25 m. Water samples were collected with a Van Dorn sampler from the second vessel and analyzed for SSC. The corresponding turbidity output from the profiler at the nearest vertical location was related to the time of the water sample to generate a turbidity-SSC calibration curve. Turbidity output was then converted to SSC.

All profiling data were linearly interpolated spatially and temporally to the same transect path, vertical bins, and times of the ADCP measurements. Final interpolated grids were cross-checked with the original Seabird profiles to ensure that errors were not generated in the interpolation process. The cross-sectional distributions of SSC can be balanced laterally and vertically to determine the center of mass in the cross-section for a given time.

2.3. Results

2.3.1. Continuous monitoring

Point SSC in the four quadrants was successfully measured for 28 days (Fig. 4). Inspection of the time-series reveals substantial lateral and vertical variability in SSC. At both sites, mean SSC at the lower sensor was over twice that of the upper sensor. On a tidal timescale, the water column was relatively well-mixed on strong tides, though vertical stratification was evident during neap tides. Laterally, SSC at site SBen peaked at the start of flood tide, while site NBen experienced peak SSC at the end of ebb tide (Fig. 5). Velocity data at site NBen was obtained for the entirety of the record, while the instrument at site SBen was tipped over on May 30, 2004, leading to a loss of the data for the remainder of the deployment. Velocity data at both sites shows increased gravitational circulation during neap tides.

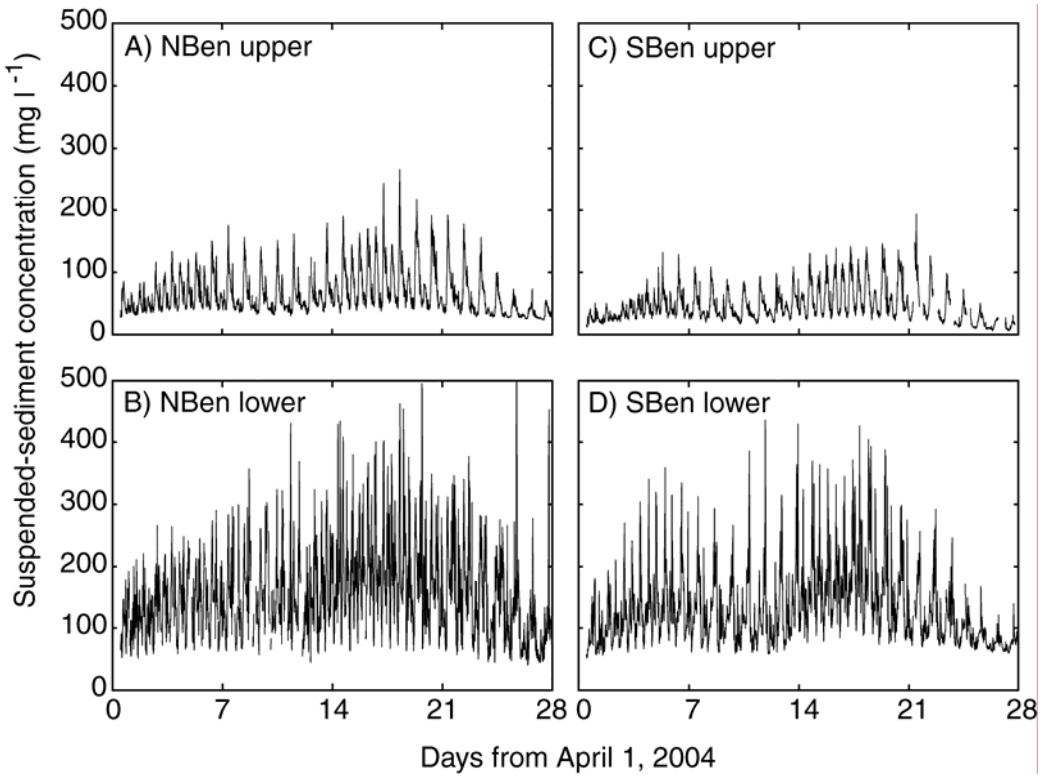

Figure 4. Time-series of SSC from four optical sensors at cross-section in Carquinez Strait: A) upper sensor at site NBen; B) lower sensor at site SBen; C) upper sensor at site SBen; and D) lower sensor at site SBen.

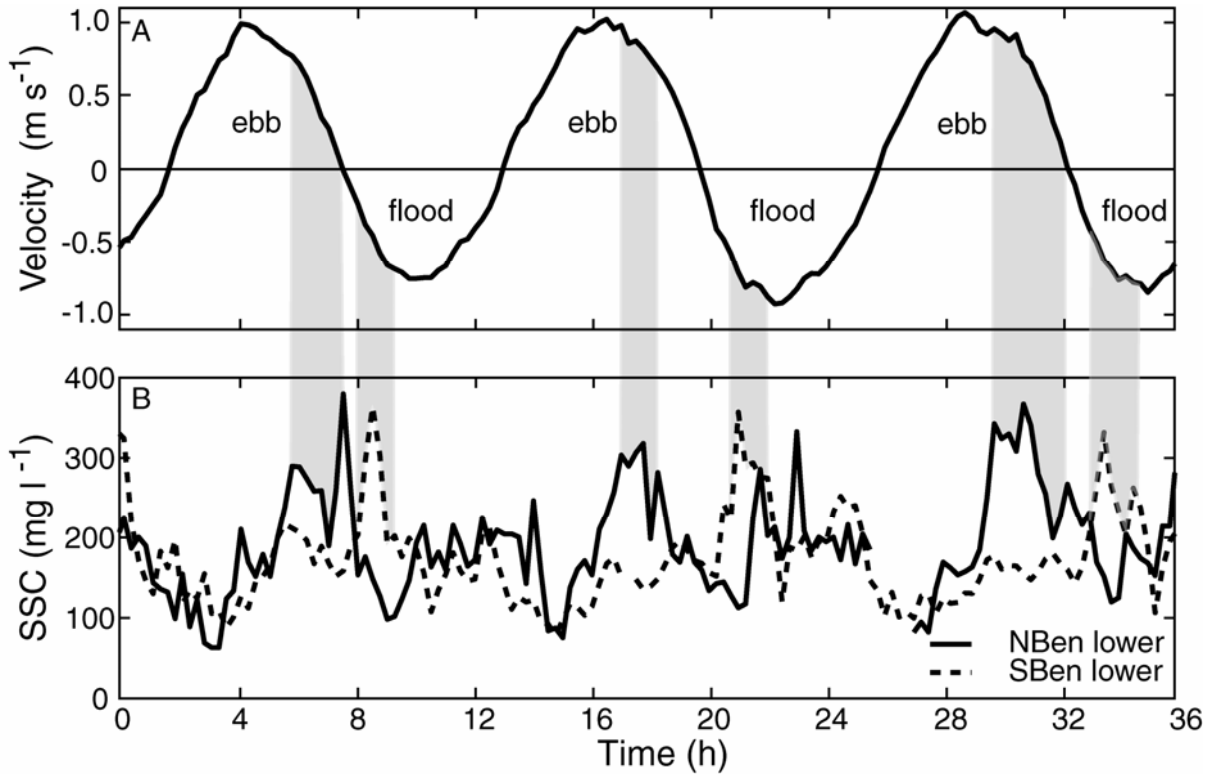

Figure 5. Time-series of A) mean velocity in Carquinez Strait and B) SSC from lower sensors at sites NBen (solid) and SBen (dashed). SSC at SBen is typically maximum at the start of flood, while SSC at NBen is maximized at the end of ebb.

Results from the center of mass calculations demonstrate large variability in lateral and vertical position on the tidal timescale (Fig. 6). The center of mass calculation results in a northerly position when SSC is greatest on the north side, and vice-versa. The northern-most position on the tidal timescale was 125 m north of center, while the southern-most position was 100 m south of center. On a tidally averaged basis, these fluctuations are reduced to 40 m north of center (northern-most) and 8 m north of center (southern-most). The maximum tidally averaged north position occurs during a neap tide, while the maximum southern position occurs during a spring tide. Vertically, the maximum and minimum instantaneous vertical positions were 7 and 4 m above the lower sensors, respectively, while the tidally averaged maximum and minimum positions were 5.5 and 4.75 m respectively.

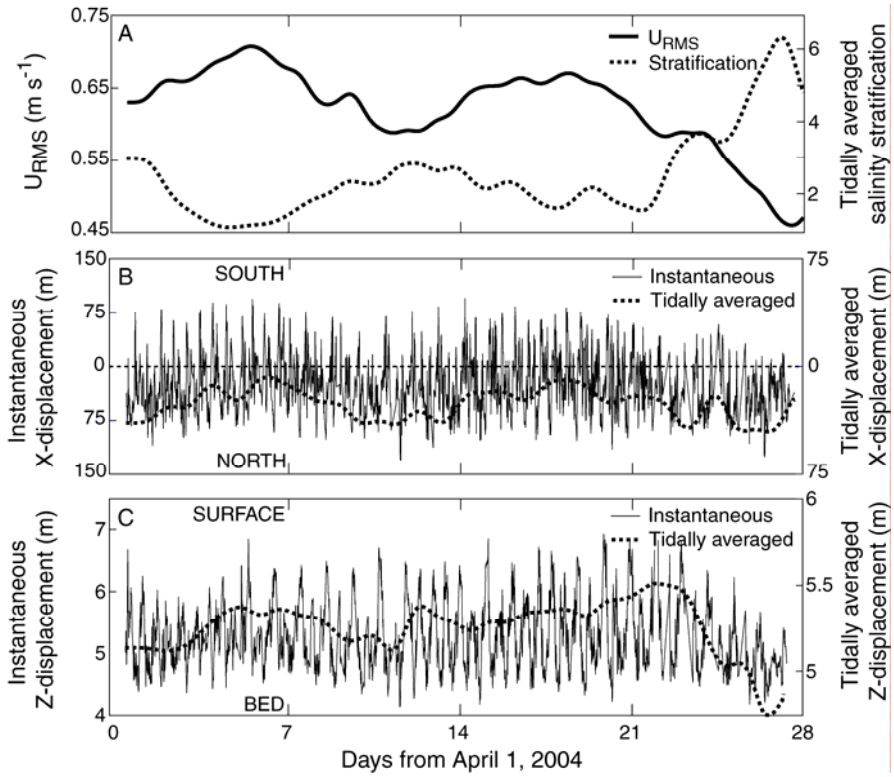

Figure 6. Time-series of A) tidal energy (U_{rms}) and tidally averaged stratification in Carquinez Strait; B) x-displacement of the ETM center of mass; and C) y-displacement of the ETM center of mass. Center of mass favors the north side and lower water column on neap tides during periods of reduced tidal energy, and migrates toward the south side and upper water column on spring tides during periods of increased tidal energy.

2.3.2. Tidal cycle monitoring

The tidal-cycle, cross-sectional measurements validate the large lateral and vertical variability observed in the time-series of point SSC. On early ebb tide, velocity in the northern half of the channel led by 30 min over the southern half, which was still slightly flooding. As the entire channel turned to ebb, SSC was greatest on the north side of the channel (SSC>300 mg l^{-1}), leading to a northerly ETM center of mass (Fig. 7, circles 1,2,3). The transition from ebb to flood was characterized by greater SSC on the south side and in the lower water column (SSC >1000 mg l^{-1}), leading to a center of mass that moved southward (Fig. 7, circles 4, 5). As flood tide progressed, the center of mass moved towards the center of the channel, but back southward at maximum flood tide (Fig. 7, circle 7). Over this 12 h period, the center of mass varied 250 m laterally and 5 m vertically. Maximum northern position occurred on maximum ebb tide, while maximum southern position occurred at slack after ebb. The minimum vertical position occurred on slack tides due to deposition, while maximum vertical position occurred during maximum velocities.

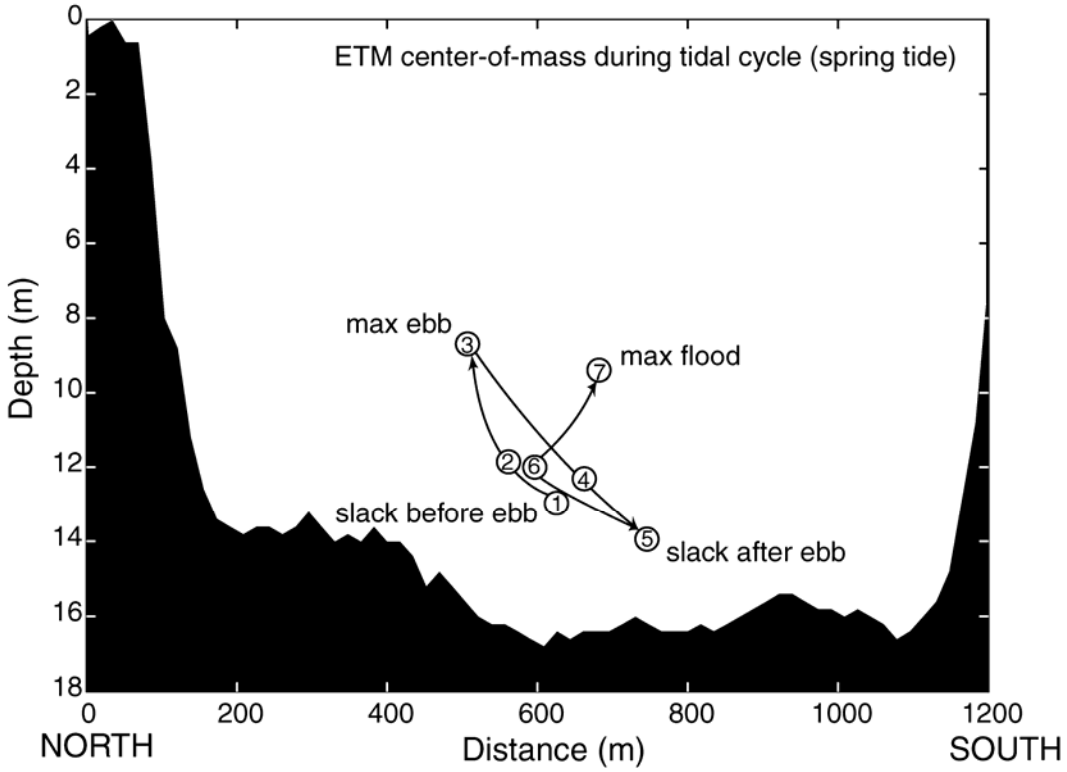

Figure 7. Movement of ETM center of mass between slack before ebb to max flood, obtained by water column profiling of SSC in the transect seaward of the I-680 Bridge (Fig. 2). Center of mass begins at circle marked 1 at slack before ebb, migrates to 3 at maximum ebb, 5 at slack after ebb, and 7 at maximum flood tide. Depth is referenced to mean lower low water.

The highly variable bathymetry of the Strait seaward of the I-680 Bridge precludes direct comparison of the data from the three cross-sections (i.e. the I-680 Bridge, the ADCP-occupied cross-section, and the tidal-cycle profiling transect). The I-680 Bridge cross-section (Fig. 3) shows the north side as the deeper side, whereas the tidal-cycle monitoring cross-section (Fig. 7) shows the south side as the deeper side. The deeper section runs across the Strait in this fashion, and therefore it is difficult to articulate the dynamics between the three cross-sections.

3. Modeling simulations

While the mechanism of vertical ETM displacement is increased tidal energy (which leads to enhanced vertical mixing), the mechanism for lateral ETM displacement is not obvious from the observations. Lateral displacement is linked with tidal energy, and this may be due to secondary circulation, vertical dynamics, or local variations in bed storage of sediment. Deciphering the dominant mechanisms may be accomplished with a three-dimensional hydrodynamic/sediment transport model.

3.1. Model description

The public-domain Regional Oceanic Modeling System (ROMS, ver. 2.2) was selected for this study (Shchepetkin and McWilliams, 2005). The model solves the Reynolds-averaged Navier-Stokes equations, splitting the barotropic and baroclinic solutions into fast and slow time steps, respectively. Numerous options are available for advection and turbulence closure; third-order upstream advection (momentum and tracers) and the k-epsilon turbulence closure were selected. The domain is discretized with horizontal orthogonal curvilinear coordinates and stretched, terrain-following vertical coordinate. Modeling was performed on a 3.2 GHz desktop computer, with a 30 s time step. The model is allowed to spin-up over a two-week period, enabling salinity and velocity fields to reach an appropriate initial condition.

3.2. Methods

3.2.1. Modeling domain

The modeling domain of Suisun Bay is constrained between Carquinez Strait on the west and the Delta on the east (Fig. 8). The domain was discretized into a 160 x 87 x 8 cell domain (in the west-east, north-south, and vertical directions respectively). The geometric complexity of the Delta presents a modeling challenge: the sinuous network of channels and flooded islands requires substantial computational effort and bathymetric data. Simplification was accomplished by representing the Delta as a uniform channel (not shown). This "pseudo-Delta" was extended 80 km, which is the same length as the lower Sacramento River up to its bi-directional flow limit (Freeport, not shown). The area of the pseudo-Delta is equal to the open water area of the actual Delta. This idealization not only reduces computational effort, but it allows for simplified eastern boundary conditions. While this may introduce unrealistic conditions within the Delta, the goal is to represent conditions within Suisun Bay (and Carquinez Strait) adequately. If hydrodynamic and salinity conditions in Suisun Bay are modeled adequately, then the sediment dynamics should be unaffected by the simplification of the Delta.

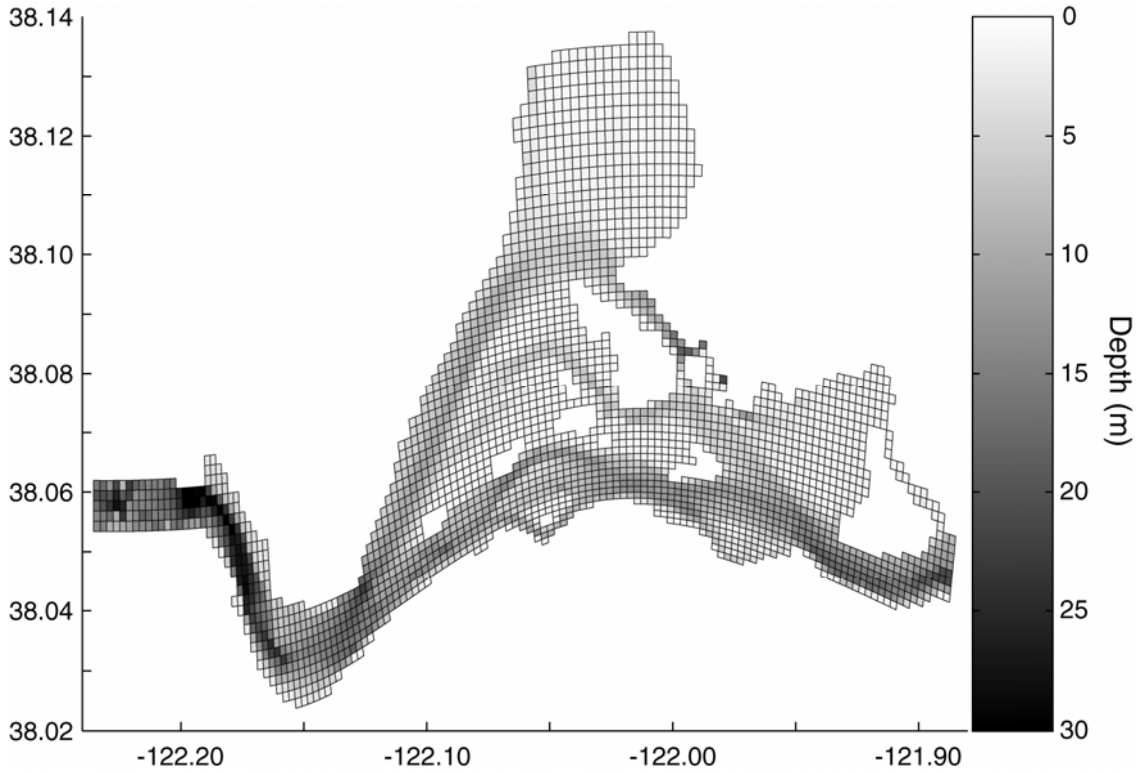

Figure 8. Computational grid of Suisun Bay, in ROMS orthogonal, curvilinear format. Depth is referenced to mean lower low water.

3.2.2. Boundary conditions

3.2.2.1. Freshwater flow, salinity, SSC: Eastern boundary conditions

Extending the pseudo-Delta to Freeport allows for the application of a unidirectional seaward transport boundary condition. The net seaward transport was obtained from Dayflow model output (California Department of Water Resources, 2005). Dayflow is an idealized representation of freshwater flow into the Delta, that accounts for water exports and diversions within the Delta. The boundary condition imposed on the eastern end allows for the tide to freely propagate out of the domain, yet maintains a prescribed freshwater transport. Salinity is zero on the eastern boundary as salt intrusion has not been observed at Freeport in the modern era of controlled flows.

Daily SSC data are available at Freeport from the U.S. Geological Survey. SSC from the San Joaquin River are assumed to be equivalent to the Sacramento River. Flow magnitude in the San Joaquin River is typically 20% of the Sacramento River flow magnitude, so this simplification is relatively minor.

3.2.2.2. Tidal flow, salinity, SSC: Western boundary conditions

Tide levels from the California Department of Water Resources Martinez station (Fig. 2) were used at the western boundary, by shifting and amplifying using tidal predictions. This is preferred to using predictions for the area near the western boundary alone; the record from the Martinez station retains sub-tidal fluctuations in water level due to atmospheric forcing (e.g. wind, pressure). As an option, ROMS calculates tidal velocities based on the tidal stage time-series. For salinity, the method of Warner et al. (2005) can be used. This is an analytical function based on near-bottom longitudinal salinity profiles as follows:

$$S(X) = (S_0/2)\,[1 + \tanh(\alpha - X/\beta)] \quad (1)$$

Where S is the salinity, X is the longitudinal coordinate with origin at the mouth of the estuary, S_0 is the seaward boundary value of salinity (held at 30, due to tidal variability), and α, β are empirical parameters. Parameter α is held constant as 2 following Warner et al. (2005). The parameter β is related to freshwater flow (Q); for a given estuary this relationship can be established and used in the analytic expression. Data from 358 longitudinal cruises of the *R/V Polaris* were processed to determine this relationship ($\beta = \exp[4.25 - 0.22 \log Q]$). The model then uses the derivative of Eq. 1 to determine the local salinity gradient. The salinity at the open boundary is computed with the local salinity gradient value and the first interior salinity value. The model was initialized with a longitudinal salinity distribution based on observations to accelerate convergence. The initial vertical salinity distribution is uniform.

The western SSC condition was specified as the velocity-weighted SSC at the I-680 Bridge. This value was computed and estimated using SSC measured at the four sensors mounted on the I-680 Bridge (Ganju and Schoellhamer, 2006). The model code for this simulation was modified to compute the flood-tide velocity at the boundary, distribute the flood-tide SSC in a Rouse profile, and ensure that the final velocity and SSC product matches the value estimated at I-680 Bridge. This assumes negligible erosion and deposition within Carquinez Strait.

3.2.3. Calibration and validation

Calibrating to stage at the western and eastern ends of Suisun Bay (Martinez and Mallard Island, respectively, Fig. 2) was deemed a sufficient goal for these simulations. The bottom logarithmic drag coefficient was varied to achieve the optimum agreement between observations and model simulations. Observations of stage were available from the California Department of Water Resources for gages situated at Martinez and Mallard Island, though data were sparse between April 1 and April 28, 2004. Calibration results will be extended to May 4, 2004, to yield an adequate comparison. Calibration to sediment data are not necessary, as we wish to qualitatively identify the ETM movement mechanisms, which should be independent of sediment concentration.

Validation will be evaluated with regards to vertical and longitudinal salinity gradients. The dynamics of salinity are known to be critical for sediment transport within Suisun Bay and Carquinez Strait. Both longitudinal and vertical salinity gradients can alter the sediment transport direction and magnitude. The longitudinal gradient is defined as the difference in near-bottom salinity between site NBen and Mallard Island, while the vertical stratification is defined as the difference between near-bottom and mid-depth salinity at site NBen.

3.2.4. Center of mass calculation

ROMS uses a stretched vertical and curvilinear horizontal coordinate, therefore the mass of sediment in each cell was computed and applied at the center of each cell. The center of mass was then determined by balancing sediment mass in the vertical and horizontal.

3.3. Results

3.3.1. Calibration and validation

Calibration to stage was accomplished with an r^2 above 0.99 at both Mallard Island and Martinez (Fig. 9), by modifying the bottom roughness in the log-drag stress formulation (z_o=0.004 m). The time-series of vertical salinity structure (Fig. 10, tile A) showed a satisfactory pattern of greater stratification on neap tides, and increased mixing on spring tides, though the model results deviate from observations. Similarly, the tidal variability and relative amplitude of the longitudinal salinity gradient are in agreement with observations, but the absolute values are not modeled well (Fig. 10, tile B). The instantaneous time-series of salinity dynamics are not as well-matched to observations; this is most likely due to the salinity boundary condition which is solved as a function of freshwater flow. The use of this function is justified, however, due to limited salinity data at the western boundary; in addition, further investigations will require historical boundary conditions (when flow data were available but salinity data were not).

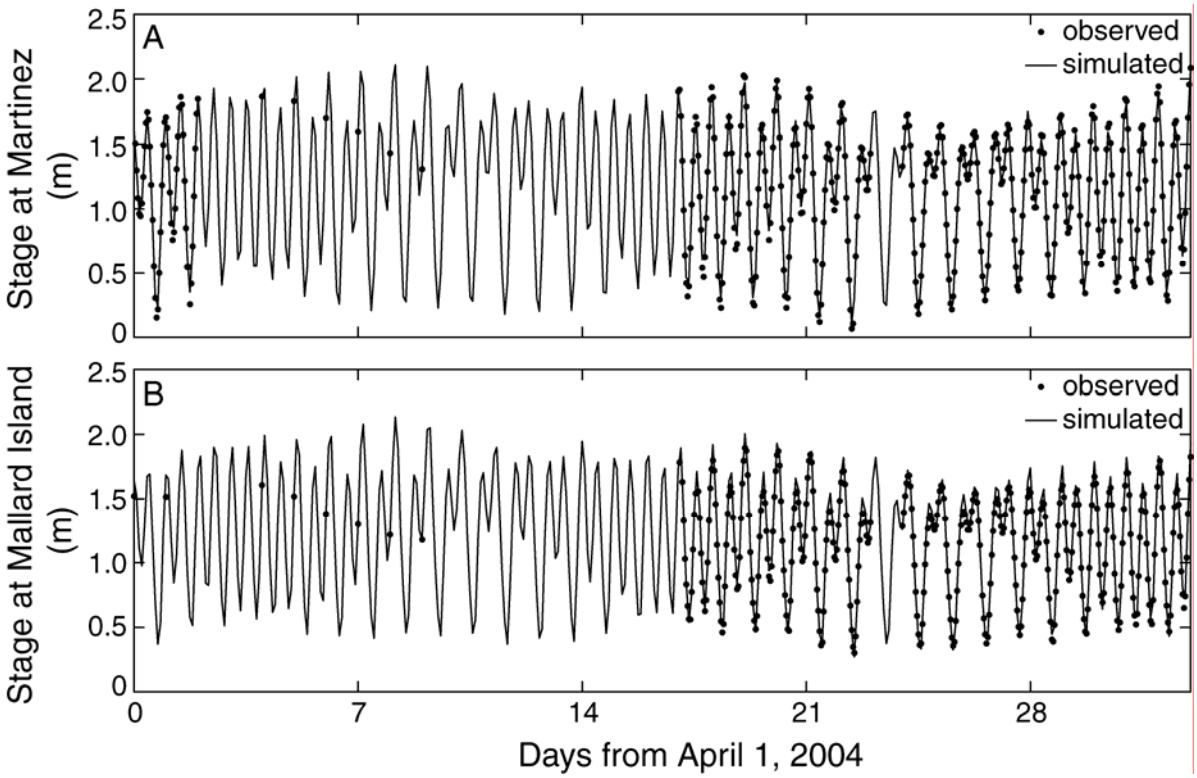

Figure 9. Model calibration to stage at A) Martinez and B) Mallard Island. The two sites represent the western (Martinez) and eastern (Mallard Island) ends of Suisun Bay. Stage is referenced to mean lower low water.

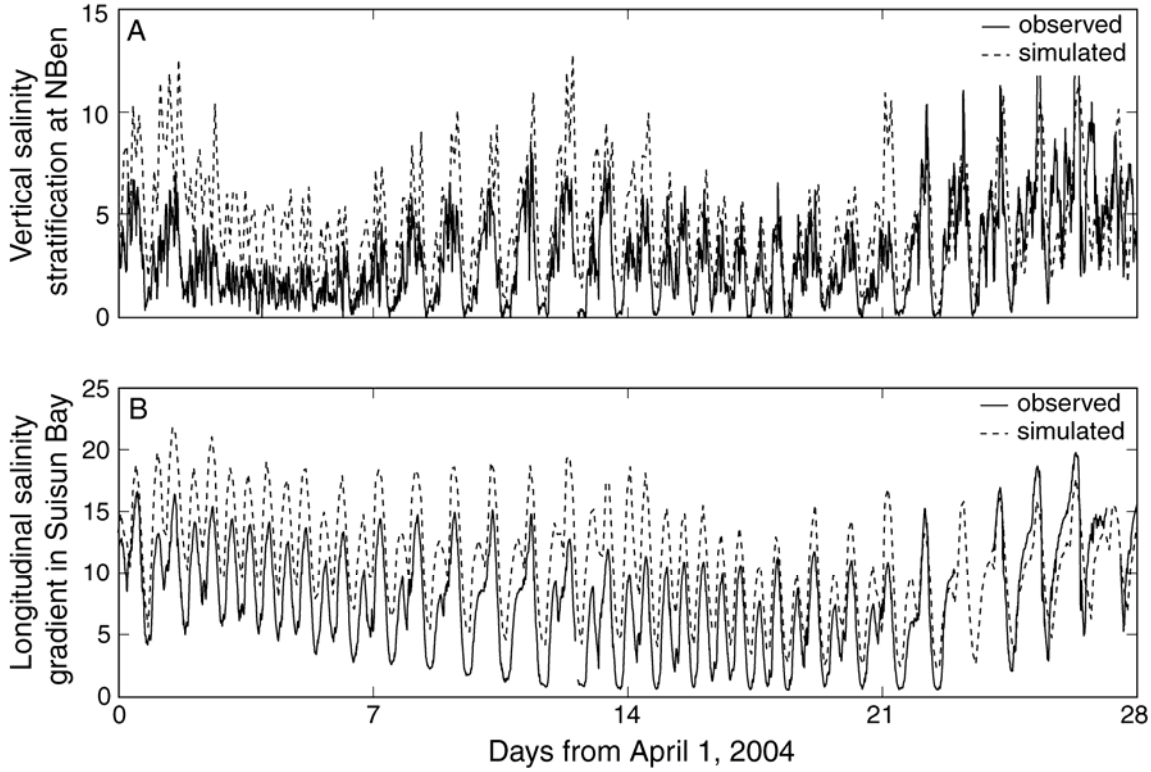

Figure 10. Model validation to A) vertical salinity stratification at site NBen and B) longitudinal salinity gradient between site NBen and Mallard Island.

3.3.2. Center of mass calculation

The center of mass of the entire ETM varied in response to tidal energy and vertical stratification in the same manner as the observations (Fig. 11). Reduced tidal energy led to increased vertical stratification, and a northerly ETM position (Fig. 11, tile B). Increased energy and reduced stratification displaced the ETM position to the south. Instantaneous displacements were as large as 200 m in the lateral and 4 m in the vertical, while tidally averaged displacements ranged from 50 m to 1 m in the lateral and vertical, respectively. These displacements are in agreement with the observed displacements, despite the limitations of the four sensor method (i.e. incomplete representation of entire cross-section). We do not compare the absolute values of the field and modeling observations, as the coordinate system origins and domains are not congruent.

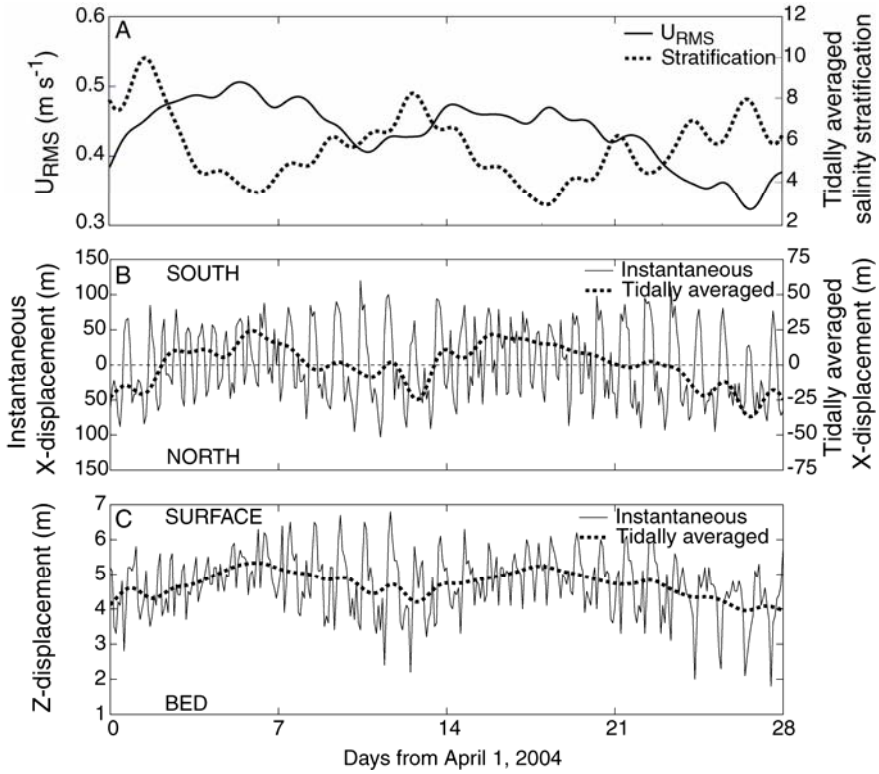

Figure 11. Model results of A) tidal energy (U_{rms}) and tidally averaged stratification; B) x-displacement of the ETM center of mass; and C) y-displacement of the ETM center of mass. In agreement with field observations, center of mass favors the north side and lower water column on neap tides during periods of reduced tidal energy, and the south side and upper water column on spring tides during periods of increased tidal energy.

4. Discussion

The existing conceptual model of the ETM in Carquinez Strait (Schoellhamer and Burau, 1998) stresses the importance of topography in controlling gravitational circulation. A topographical control that restricts gravitational circulation allows for the trapping of particles near the bed. During neap tides, persistent stratification inhibits vertical mixing, and near-bed SSC is maximized.

In a 2D laterally averaged sense, two conceptual models are applicable to Carquinez Strait. The north side, with an abrupt bathymetric change from 18 m to 11 m, follows the Schoellhamer and Burau (1993) conceptual model for ETM formation. When the south side is considered, it is clear that the lack of a topographical control does not promote local particle trapping. Therefore the cross-section behaves as a combination of two separate 2D conceptual models: one with a topographical control, one without. The transition between spring and neap tides leads to an analogous transition for ETM position. Gravitational circulation, stratification, and particle trapping are enhanced on the north side during neap tides, displacing the ETM to the north, while a reduction in the strength of these mechanisms during spring tides displaces the ETM towards the south.

The simulation results reflect this conceptual model in a 2D vertically averaged sense. The product of mean surface (u_s) and near-bottom (u_b) residual currents yields an estimate of gravitational circulation strength (Fig. 12, tile A). When the product is large and negative, this indicates strengthened gravitational circulation; a near-zero or positive product indicates a lack of gravitational circulation. On neap tides the strength is increased west of the topographical control, yet abruptly decreases eastward on the north side while gradually decreasing eastward on the south side. This indicates the trapping mechanism on the north side, seaward of the topographical control. The change in gravitational circulation strength from spring to neap (Fig. 12, tile B) shows a greater increase in strength (more negative) in the north as opposed to the south (at the I-680 Bridge transect). On the south side, strength is increased landward and seaward of the I-680 Bridge, therefore particles are not trapped in this region.

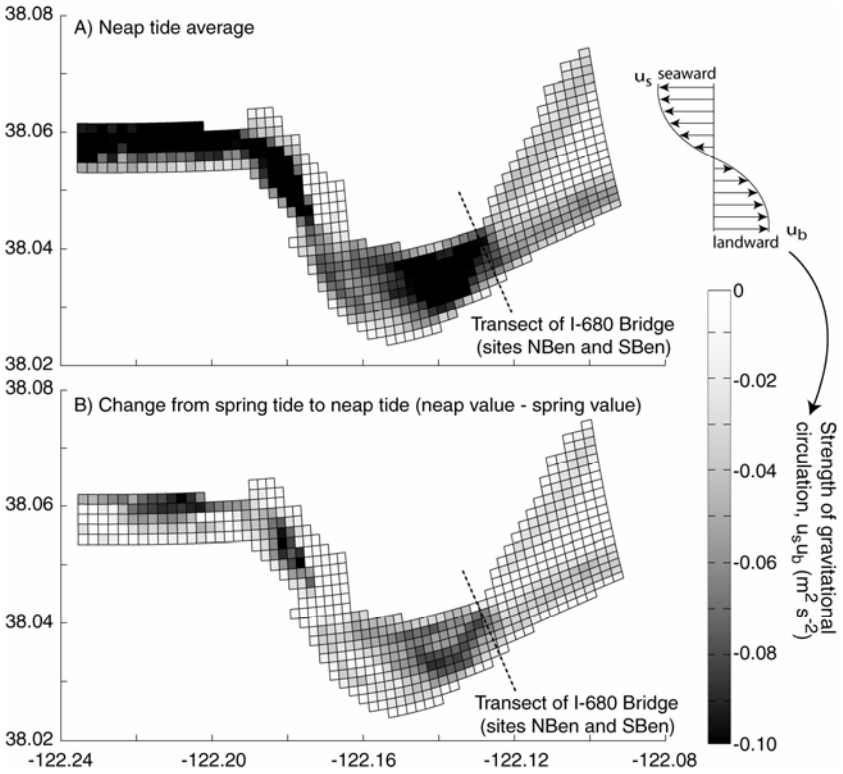

Figure 12. Model surface plot of A) strength of gravitational circulation on neap tide and B) change in strength from spring tide to neap tide. Increasingly negative values indicate larger negative product of surface and bottom velocities, and therefore stronger gravitational circulation.

Secondary currents in Carquinez Strait are evident in ADCP data from both the boat and bottom-mounted units. The configuration of Carquinez Strait, with a prominent bend and variable topography, promotes secondary circulation on both spring and neap tides. Simulation results (Fig. 13) show strengthening of this circulation during spring tides, due to higher tidal velocities. A prominent counter-clockwise gyre between sites NBen and SBen is active on spring tides and weakened on neap tides. This gyre delivers near-bed water from the northwest to the southeast, and a complementary transferal of surface waters from southeast to northwest. Particle trapping on the north side during neap tides is suggested by previous work (Schoellhamer and Burau, 1998) and the work presented here. Therefore there is a temporary storage of sediment on the bed of the north side, during neap tides. The ensuing spring tide transports sediment from this temporary deposit and secondary circulation tends to deflect sediment-rich, near-bed water to the southeast, displacing the ETM center of mass southward.

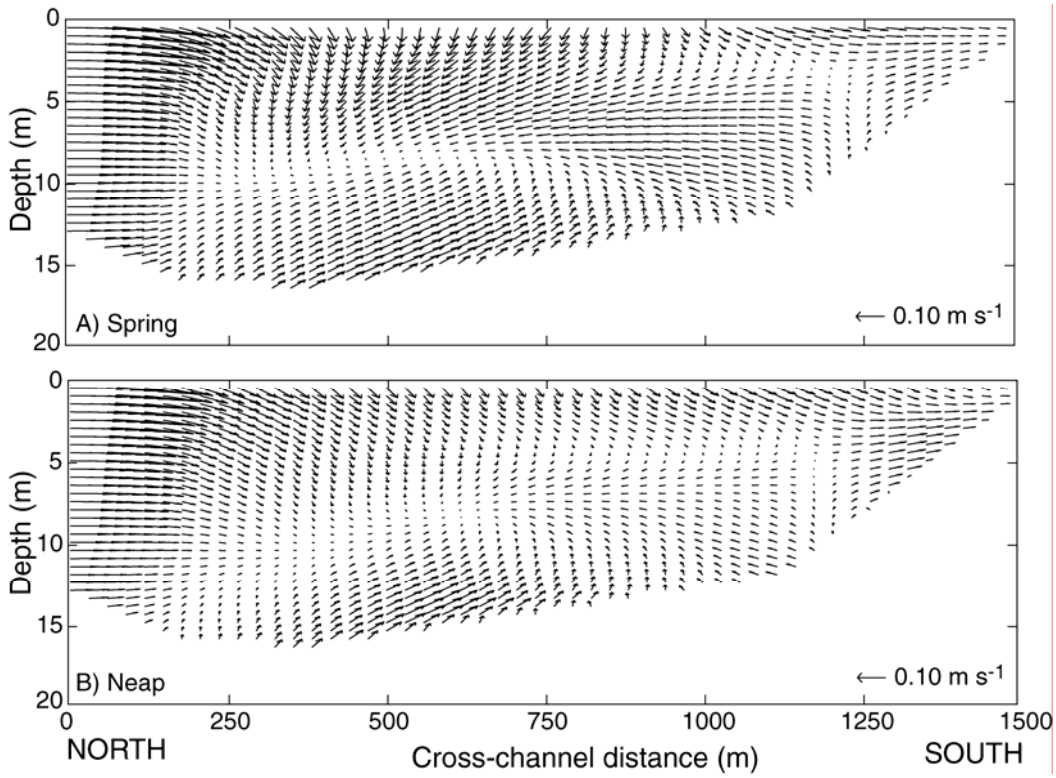

Figure 13. Modeled cross-channel and vertical velocity vectors on A) spring tide and B) neap tide. Lateral and vertical circulation are enhanced on spring tide, with near-bed velocities on the north side directed southward. Depth is referenced to mean lower low water.

5. Conclusions

The lateral position of a longitudinally fixed ETM in a tidal strait is not a constant, steady value. The center of mass moves coherently in response to tidal energy, stratification, and gravitational circulation. Field and modeling observations indicate that the lateral position can change by as much as 250 m in a 1200 m channel on the tidal timescale (20% of width), and 50 m on a tidally averaged basis. Vertical position expectedly responds to vertical mixing, with position varying by 5 m on the tidal timescale (17% of depth) and 1 m on the tidally averaged timescale. Gravitational circulation and bathymetry clearly affect the movement and trapping of particles, modulating the center of mass of the ETM. Secondary circulation in the channel distributes sediment on energetic tides, also displacing the center of mass. When combined, these mechanisms are all responsible for the lateral movement of the ETM, in a relatively narrow and energetic tidal strait. In wider estuaries, the lateral variability may be even more dramatic, due to lateral variations in tidal energy, stratification, and temporary sediment storage. In the case of a longitudinally varying ETM, the lateral and longitudinal positions may be correlated as well. The lateral position of an ETM may affect lateral gradients in deposition, contaminant uptake to the food web, and benthic community composition.

Acknowledgments

This work was paid for in part with funds from California State Water Resources Control Board contract #01-281-150-2. Tidal-cycle measurements were performed with the assistance of Curt Battenfeld, Greg Brewster, Paul Buchanan, Jay Cuetara, Megan Lionberger, Heather Ramil, Greg Shellenbarger, and Brad Sullivan. ADCP data were analyzed by Randal Dinehart. Jon Burau supplied invaluable input concerning the hydrodynamics of the area. John Warner provided indispensable assistance with model development/application, and Aaron Blake provided a helpful review of the manuscript.

References

Aller, J.Y., and Stupakoff, I., 1996. The distribution and seasonal characteristics of benthic communities on the Amazon shelf as indicators of physical processes. Continental Shelf Research 16, 717–751.

Buchanan, P.A., Ganju, N.K., 2005. Summary of suspended-sediment concentration data in San Francisco Bay, California, water year 2003. U.S. Geological Survey Data Series 113.

Burau, J.R., Simpson, M.R., and Cheng, R.T., 1993. Tidal and residual currents measured by an acoustic Doppler current profiler at the west end of Carquinez Strait, San Francisco Bay, California, March to November 1988. U.S. Geological Survey Water-Resources Investigations Report 92-4064, 79 p.

California Department of Water Resources, 2005. DAYFLOW program documentation and DAYFLOW data summary user's guide. http://iep.water.ca.gov/dayflow

Ganju, N.K., and Schoellhamer, D.H., 2006. Annual sediment flux estimates in a tidal strait using surrogate measurements. Estuarine, Coastal and Shelf Science 69, 165–178.

Ganju, N.K., Schoellhamer, D.H., Warner, J.C., Barad, M.F., and Schladow, S.G., 2004. Tidal oscillation of sediment between a river and a bay: a conceptual model. Estuarine, Coastal and Shelf Science 60, 81–90.

Geyer, W.R., Signell, R.P., and Kineke, G.C., 1998. Lateral trapping of sediment in a partially mixed estuary. In: 8th Biennial Conference on Physics of Estuaries and Coastal Seas, 1996. A. A. Balkema, Rotterdam, The Netherlands, pp. 115–126.

Grabemann, I., Uncles, R.J., Krause, G., and Stephens, J.A., 1997. Behaviour of turbidity maxima in the Tamar (U.K.) and Weser (F.R.G.) Estuaries. Estuarine, Coastal and Shelf Science 45, 235–246.

Islam, M.S., Ueda, H., and Tanaka, M., 2005. Spatial distribution and trophic ecology of dominant copepods associated with turbidity maximum along the salinity gradient in a highly embayed estuarine system in Ariake Sea, Japan. Journal of Experimental Marine Biology and Ecology 316, 101–115.

Jay, D. A., and Musiak, J.D., 1994. Particle trapping in estuarine turbidity maxima. Journal of Geophysical Research 99, 446–461.

Kimmerer, W.J., Burau, J.R., and Bennett, W.A., 1998. Tidally oriented vertical migration and position maintenance of zooplankton in a temperate estuary. Limnology and Oceanography 43, 1697–1709.

Sanford, L.P., Suttles, S.E., and Halka, J.P., 2001. Reconsidering the physics of the Chesapeake Bay estuarine turbidity maximum. Estuaries 24, 655–669.

Schoellhamer, D.H., 2001. Influence of salinity, bottom topography, and tides on locations of estuarine turbidity maxima in northern San Francisco Bay. In: Coastal and Estuarine Fine Sediment Transport Processes, W.H. McAnally and A.J. Mehta eds., Elsevier Science B.V., pp. 343–357.

Schoellhamer, D.H., and Burau, J.R., 1998. Summary of findings about circulation and the estuarine turbidity maximum in Suisun Bay, California. U.S. Geological Survey Fact Sheet FS-047-98, 6 p.

Shchepetkin, A.F., and McWilliams, J.C., 2005. The regional oceanic modeling system (ROMS): a split-explicit, free-surface, topography-following-coordinate oceanic model. Ocean Modelling 9, 347–404.

Warner, J.C., Geyer, W.R., and Lerczak, J.A., 2005. Numerical modeling of an estuary: a comprehensive skill assessment. Journal of Geophysical Research, 110, C050001.

Woodruff, J.D., Geyer, W.R., Sommerfield, C.K., and Driscoll, N.W., 2001. Seasonal variation of sediment deposition in the Hudson River estuary. Marine Geology 179, 105–119.